



Repositorio Institucional de la Universidad Autónoma de Madrid

<https://repositorio.uam.es>

Esta es la **versión de autor** del artículo publicado en:

This is an **author produced version** of a paper published in:

Nanoscale 10.2 (2018): 705-715

DOI: <http://doi.org/10.1039/c7nr04304j>

Copyright: © The Royal Society of Chemistry 2018

El acceso a la versión del editor puede requerir la suscripción del recurso

Access to the published version may require subscription

Experimental Evidence of Charged Domain Walls in Lead-free Ferroelectric Ceramics: Light-driven Nanodomain Switching†

Fernando Rubio-Marcos^{†,*}, Adolfo Del Campo[‡], Rocío E. Rojas-Hernandez^{†,¶}, Mariola O. Ramírez[§], Rodrigo Parra[‡], Rodrigo U. Ichikawa[#], Leandro A. Ramajo[‡], Luisa E. Bausá[§] and Jose F. Fernández[†].

[†] *Electroceramic Department, Instituto de Cerámica y Vidrio, CSIC, Kelsen 5, 28049 Madrid, Spain*

[¶] *Departamento de Engenharia Química/CQE, Instituto Superior Técnico/UL, Lisboa, Portugal*

[§] *Department of Física de Materiales and Instituto Nicolás Cabrera, Universidad Autónoma de Madrid, 28049 Madrid, Spain*

[‡] *Instituto de Investigaciones en Ciencia y Tecnología de Materiales (INTEMA), Av. Juan B Justo 4302 (B7608FDQ), Mar del Plata, Argentina*

[#] *Instituto de Pesquisas Energéticas e Nucleares, IPEN-CNEN/SP, Butantã, São Paulo, SP, 05508-000, Brazil*

*Correspondence and requests for materials should be addressed to F. R-M (email: frmarcos@icv.csic.es)

ABSTRACT: The control of ferroelectric domain-walls at the nanometric level leads to novel interfacial properties and functionalities. Especially, the comprehension of charged domain walls, CDWs, lies at the frontier of future nano-electronic research. Whereas many of the effects has been demonstrated for ideal archetypes, such as single crystals, or/and thin films, similar control of CDWs on polycrystalline ferroelectrics has not been achieved. Here, we unambiguously show the presence of charge domains walls on a lead-free (K,Na)NbO₃ polycrystalline system. The appearance of CDWs is observed *in situ* by confocal Raman microscopy and second harmonic generation microscopy. CDWs produce an internal strain gradient within each domain. Specifically, the anisotropic strain develops a crucial piece in the ferroelectric domain switching due to the coupling between the polarization of light and the ferroelectric polarization of the nanodomain in the (K,Na)NbO₃ ceramic. This effect leads to the tuning of ferroelectric domain switching by means of light polarization angle. Our results will help to understand the relevance of charge domains walls on ferroelectric domain switching process and may facilitate the development of domain wall nanoelectronics by remote light control utilizing polycrystalline ferroelectrics.

Keyword: *Ferroelectric domain structure; Strain gradient; Charged domain walls; Optical-driven ferroelectric domain switching; Lead-free Piezoelectric ceramics materials*

1. Introduction

Domain structure of a ferroelectric material is determined to find harmony on the electrostatic depolarization, elastic strain, and domain wall energies. The resulting domain structure has a profound impact on the polarization switching behavior.¹⁻⁷ Overall, domains are regions in the ferroelectric material in which the order parameter (electric polarization) is oriented in one of the permitted symmetry directions.⁵⁻¹¹ Domain walls (DWs) are the interface between adjacent domains, in which their properties can be radically different from those of the domains themselves.^{2-7, 11, 12} New strategies are constantly being developed in order to find effective methodologies capable of modulating ferroelectric domain motion.^{3,4,13-16} In fact, recent studies have shown that domain walls themselves possess interesting functionalities (e.g., electronic conductivity)^{1-4,6,13-16} and have the potential for other interesting effects, making domain walls potential candidates for active elements in future nano-electronics.^{1-4,6,13-16}

One of the major limitations in ferroelectric domain switching is the required presence of electrical connections or physical contact in practical applications. Recently, *T. Sluka et al*¹⁴ demonstrated the correlation between the existence of charged domain walls (CDWs) in a BaTiO₃ (BTO) ferroelectric single crystal and their enhanced electromechanical properties by electron-gas like conductivity. The discovery of this motivating behavior and the potential technological applications from these enhanced functionalities raises the need for an efficient method to switch ferroelectric domains. For instance, the light-matter interaction process via photostriction in ferroelectrics can be exploited in photovoltaic devices.¹⁷⁻²¹ Recently, the possibility to move ferroelectric domain walls by means of coherent light has been demonstrated.¹⁶ In a proof-of-principle experiment we demonstrated that optical control of ferroelectric domain-wall is nevertheless possible in ideal archetypes, such as single crystals.¹⁶ Transfer of this concept to ferroelectric ceramic materials is appealing because of the increasing technological interest in new cost-effective optoelectronic nanodevices.

Manipulating ferroelectric domains for nanoelectronic engineering has been a hot research topic that has aroused great interest. To date, many of the effects observed in novel nanomaterials and nanotechnology are restricted to ideal archetypes, such as single crystals, or/and thin film (or nanoscale) on which it has a high degree of control over their structure, morphology and geometry. However, the latent role of nanoscale conductivity, particularly at the DWs, on domain-wall motion of polycrystalline ferroelectrics with randomly oriented grains has not been given sufficient attention so far. Indeed, despite of the well-developed TEM and PFM experiments to study the domain structure and switching in polycrystals, there are few works devoted to the occurrence of charged DW in ferroelectrics ceramics. Nonetheless, these polycrystalline materials have

important technological implications since they are used in the majority of piezoelectric mechanism because are easy to manufacture at low cost. In these systems even if the local conductivity within the DWs does average macroscopically to a small value, the dynamics of DWs may still be strongly affected by their conductivity. This effect would be relevant since domain-wall motion shows a major influence on the dielectric and piezoelectric properties of ferroelectric materials, contributing greatly to the macroscopic response.²²⁻²⁵ Therefore, the local conductivity at DWs may meddle with the domain-wall switching and, thus, indirectly influence the macroscopic response of polycrystalline ferroelectrics.

Here, we explore the relationship between the strain gradient within the ferroelectric domains and uncompensated accumulated charge in domain walls by investigating photo-induced ferroelectric domain switching in a polycrystalline sample of ferroelectric potassium–sodium niobate ($\text{K}_{0.1}\text{Na}_{0.9}\text{NbO}_3$; KNN) having monoclinic symmetry. We have stabilized a monophasic state with a domain structure consistent with a M_C monoclinic phase (space group Pm) (**Supplementary Information 1**).²⁶ So, the low-symmetry monoclinic phase contributes to accommodate the large elastic forces that develop at the morphotropic phase boundary (MPB), and provides elastic matching at the internal interfaces inducing large piezoelectricity.²⁷ We find that this strain is anisotropic into ferroelectric domains, and consequently, forms exotic dipole-charged domain walls. We also show that this strain gradient can be controlled by the angle of illuminating with polarized light. Ultimately, the methodology of the present study leads to a non-invasive (no damages are produced at the surface of the ferroelectric material) and reversible process in ferroelectric domain switching. The emergent phenomena driven by light-matter interaction may have potential applications in next generation domain wall nano-electronics utilizing polycrystalline ferroelectrics.

2.- Results and Discussion

2. 1. Identification of the Domain Structure by Confocal Raman Microscopy

The presence of crystalline phases play a key role on the functional properties of the ferroelectric ceramics, and therefore, their distribution and identification are relevant to tailor new approaches in designing new materials with improved properties. A standard identification of the orientation and crystalline structure of the ceramic sample was carried out by means of Synchrotron X-Ray Diffraction (HR-XRD) (see **Supplementary Figure S1** and **Supplementary Table 1**). The ceramic sample exhibited a monoclinic symmetry (M_C) showing two different orientations, (00l) or c -plane and (h00) or a -plane.

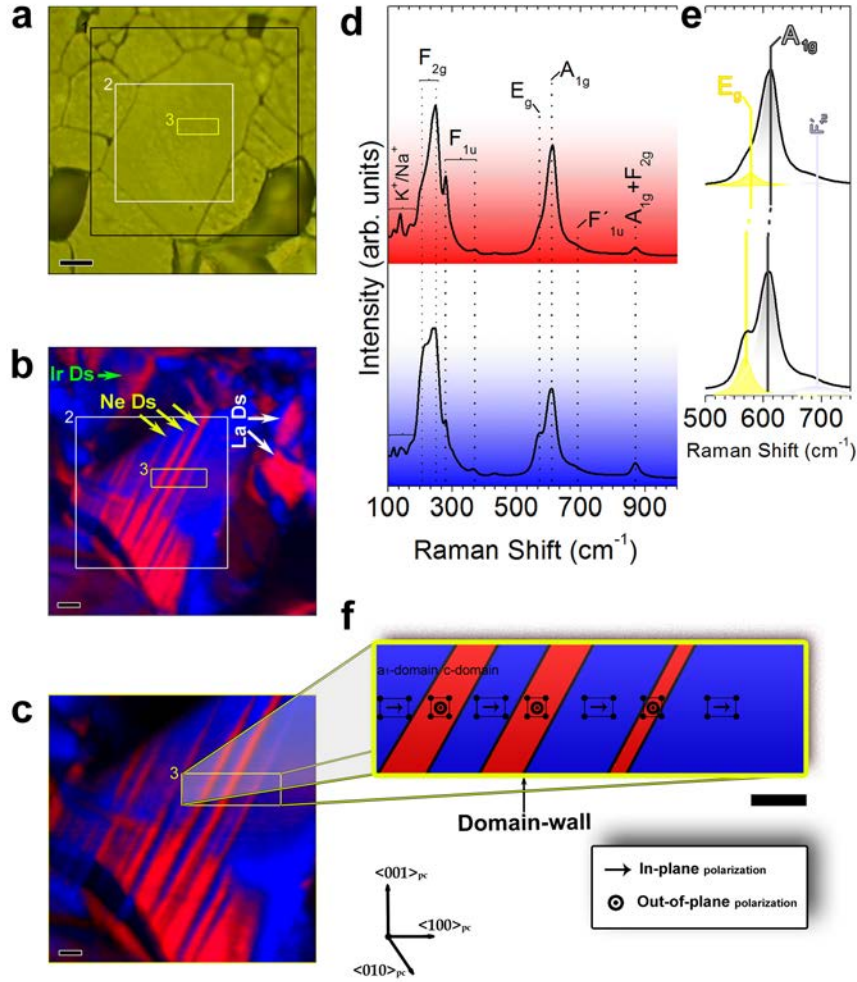


Figure 1 | Identification of the Domain Structure of a KNN Ferroelectric Ceramic by Raman Imaging (a) Optical image of the surface of (KNa)NbO₃-based polycrystalline ferroelectric. Scale bar, 4 μm. The regions marked as rectangles, and indicated as **1**, **2** and **3**, show the selected areas for XY Raman images. (b) and (c) Surface Raman images resulted from mapping the different single Raman spectra obtained from each pixel of the areas labelled as **1** and **2** in (a). Magnification increases from panel **b** to panel **c** so that scale bars in (b) correspond to 2 μm, and in (c) to 1 μm. In relation to their morphology, the domains can be categorized into different type of domains (Ds) denominated as lamellar, needle, and irregularly shaped, which are marked in panel **b** as La Ds, Ne Ds, and Ir Ds, respectively. Raman spectra showing the same spectral shift for the Raman modes are identified under same color intensity. The average Raman spectra of KNN ceramic image associated with different colours can be observed in the panel (d). (e) Amplified Raman spectra fitted by the sum of three Lorentzian peaks, ascribed to the E_g, A_{1g} and F_{1u} Raman modes, respectively. It should be taken into account that both *a*- and *c*-domains are easily evidenced by the A_{1g}/E_g ratio.²⁸ Accordingly, , panel **d** allows the identifications of *c*-domain, i.e. *out-of-plane polarization* (red spectrum), and the identifications of *a*-domain, i.e. *in-plane polarization*, (blue spectrum). (f) schematic top-view summary of the *in-plane* and *out-of-plane* polarization regions as determined by Confocal Raman Microscopy. Region marked as **3** in panels **a-c**. The sketch shows a domain structure constituted of *a*-domain and *c*-domain separated by a 90° domain wall, which are represented in blue and red colors, respectively. Scale bar, 500 nm.

Figure 1a shows an optical micrograph of the ceramic aligned perpendicular to the Raman laser. The area of 25 × 25 μm denotes the selected spatial region indicated as **1** in the panel **a**, where the Raman spectra are collected at a plane located just below the surface of the sample where the Raman intensity shows a maximum. The acquisition time for a single Raman spectrum was 200 milliseconds, thus the acquisition of a Raman image consisting of 100 × 100 pixels (10000 spectra) required 33 minutes. Features such as Raman peak intensity, peak

width or Raman shift from the recorded Raman spectra were fitted with algorithms to compare the information and to represent the derived Raman image (**Fig. 1b**). The BO_6 octahedron gives rise to 6 Raman-active modes, $A_{1g} (\nu_1) + E_g (\nu_2) + F_{1u} (\nu_3)$ being stretching modes, and $F_{1u} (\nu_4) + 1F_{2g} (\nu_5) + 1F_{2u} (\nu_6)$ bending modes.²⁸⁻³⁰ Due to the near-perfect equilateral octahedral symmetry, the A_{1g} and F_{2g} are dominant in systems similar to the one of this work.

The Raman spectra having the same Raman shift are classified by correlating the color intensity with the Raman intensity. The color assignation to each pixel results in a Raman image of the ceramic microstructure, which reveals the presence of a ceramic grain with striped ferroelectric domains. Regarding morphology, three types of domains can be recognized in KNN based ceramic: lamellar-like, needle-like, and irregularly shaped, (labelled in **Figure 1b** as La Ds, Ne Ds, and Ir Ds, respectively). In the Raman image of **Fig. 1b** a striped 90° domain structure, already reported for BaTiO_3 single crystals³¹ and PZT ceramics³² is clearly seen. In addition, a needle-like domain structure is observed, the needlepoints terminating at grain boundary. This type of domain structure has been previously reported for PbTiO_3 thin films³³, and bismuth titanate based (BiT) single crystal, and prophesied by Li et al.³⁵ The most interesting domain structure (*that is, the needle-like domains*) is basically constituted of ~ 400 nm width domains, which appear alternately (see the area marked on the yellow box and indicted as **3** in panels **a** and **b**). Through a classical approach for polycrystalline sample (ceramic), one can establish that the domain width, d , can be roughly expressed by the relation: $d \sim \sqrt{a}$ (*that is, domain widths, d , varies as the square root of the grain size, a*),^{6, 36} which implies that for grain sizes $a \sim 6.7 \mu\text{m}$ (our case) the d value should be ca. $2.5 \mu\text{m}$ (**Supplementary Information 2**). However, as we just evidenced the relevant domain structure is formed by domains with d values (~ 400 nm) significantly smaller than \sqrt{a} because of its boundary conditions, which are governed by a high internal stress. Generally, the domain size is determined by the competition between the energy of the domains and the energy of the domain walls.⁶ It is worth noticing here that the presence of a high stress is addressed by enlarging the domain walls density, resulting in a drastic reduction of the domain size as seen in **Fig. 1c**. This figure shows a magnified Raman spatial map of the domain distribution at the surface scan, which corresponds to the area marked on the white box and indicted as **2** in panels **a** and **b**. The Raman imaging shows that there are significant differences associated with the polarization orientation of each domain compatible with alternating *in plane* and *out of plane* domains, and as a result of the existence of 90° domain walls between adjacent needle-like domains. For an in-plane polarized *a*-domain, the doublet of the BO_6 octahedron stretching $E_g (\nu_2)$ and $A_{1g} (\nu_1)$ Raman modes can be observed for Raman shifts between $500\text{-}700 \text{ cm}^{-1}$; while an out-of-plane polarized *c*-domain should have only one Raman

mode corresponding to $A_{1g} (\nu_1)$ mode in this range. The experimental data further confirm the polarization orientation of each domain, as shown in **Figs. 1d-e**. In this case, as occurs in complex systems such as ceramics materials, a small contribution of the $E_g (\nu_2)$ Raman mode is observed on out-of-plane polarized c -domains due to a slight tilting of the BO_6 octahedron of the perovskite structure. See **Fig. 1e**.

In short, the CRM reveals that $(K,Na)NbO_3$ -based ceramic exhibits $a/c/a/c$ -like domains structure, which is constituted of in-plane polarized a -domains (marked in blue color) and out-of-plane polarized c -domains (signaled in red color) separated by a 90° domain wall, as shown in the scheme of the **Fig. 1f**.

2. 2. Identification of the Internal Strain Gradient within each Domain

To verify again the polarization orientation and to probe the existence of strain gradients in the $a/c/a/c$ -like domains structure, we first focus on specific relevant zones, that is on the domain walls (DWs) and on the inner region of the ferroelectric domains represented in **Figure 2a** as adjacent strip areas separated by 90° DWs.

Figure 2b shows sequential detail of the stretching $E_g (\nu_2)$ and $A_{1g} (\nu_1)$ Raman modes of the BO_6 octahedron along the different points marked in **Fig. 2a**. As has been anticipated, the A_{1g}/E_g ratio can be used to define the polarization orientation of the ferroelectric domains structure. That is, the A_{1g}/E_g ratio shows a maximum (minimum value when the coherent light polarization is perpendicular/parallel to the ferroelectric polarization, which according to our experimental configuration corresponds to the out-of-plane polarized c -domains/in-plane polarized a -domains, respectively). The evolution of the A_{1g}/E_g ratio is plotted in **Fig. 2c**.

Relative to DWs, their nature cannot be evidenced by means of the A_{1g}/E_g ratio and therefore, we need to use other relevant features as the Raman shifts that evidence chemical bond variations of the BO_6 octahedra related to the crystalline strain. Here, we use the Raman shift of the A_{1g} mode that corresponds to a symmetric vibration of the oxygen octahedra to determine the nature of the DWs. **Figure 2d** shows the Raman shift of the A_{1g} mode along the ferroelectric domain structure, which provides the local strain evolution with nanometric resolution. As observed, the Raman shift, and therefore the local strain, shows a clear oscillating trend along the $a/c/a/c$ -like domains structure, their maximum and minimum values being located close to the DWs. The alternating maxima and minima in the Raman shift of A_{1g} across the domains structure are related to a/c and c/a DWs, respectively. The a/c DWs are characterized by a Raman blueshift associated with a higher force constant for the oxygen octahedra. Meanwhile, the c/a DW's show a Raman redshift that accounts for a lower force constant of the oxygen octahedra. Accordingly, the presence of a strain gradient in the domain structure is demonstrated.

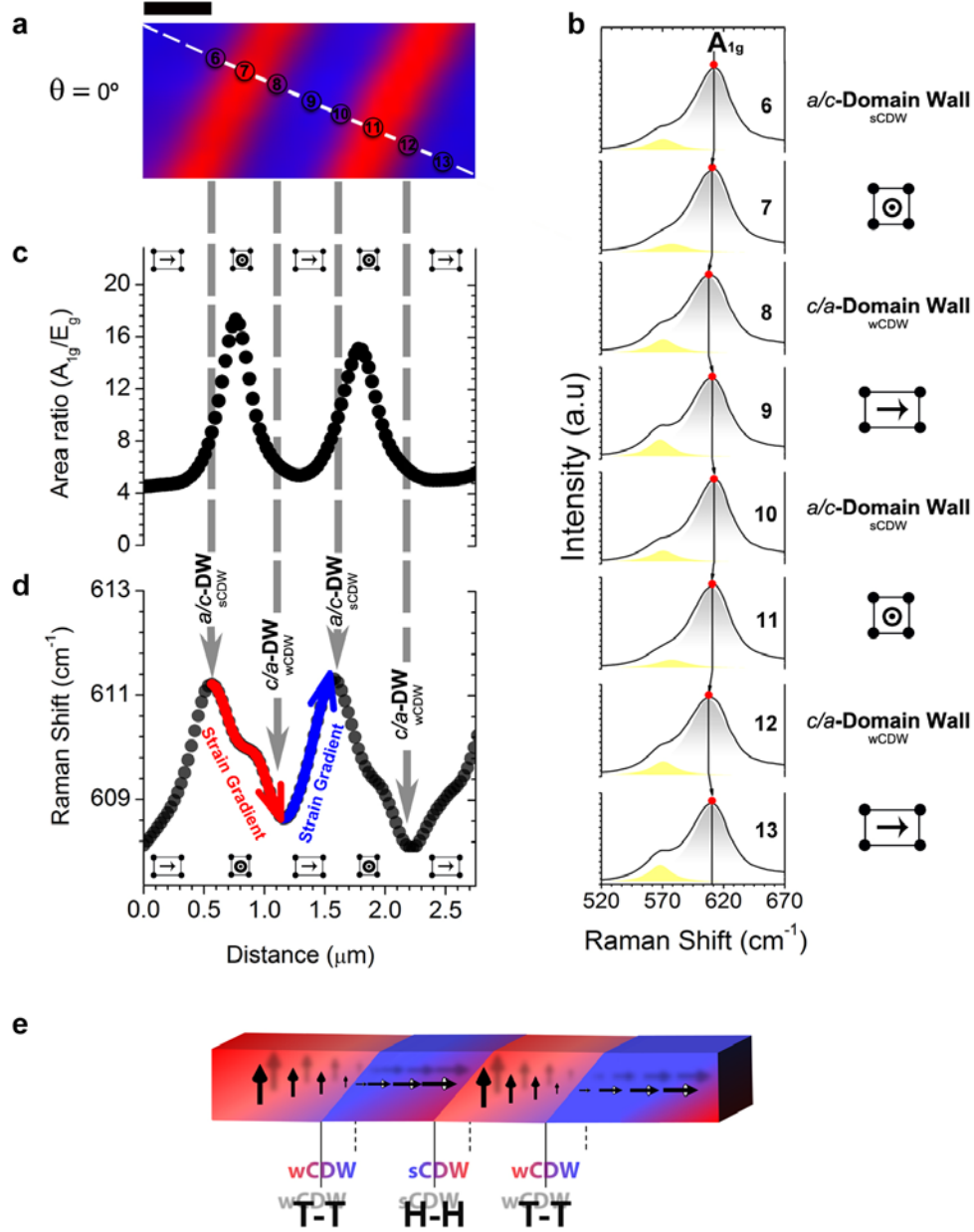


Figure 2 | Internal Strain Gradient of the Domain Structure in a KNN-based Polycrystalline Ferroelectric. (a) Raman spatial map showing the domain distribution at the surface by colour code. The circle symbols show different decisive points of the domain structure, which are associated with adjacent strip areas separated by 90° domain wall. The Raman spectra taken in these strategic points selected along x denoted as 6→13 in the panel (a). Scale bar, 500 nm. (b) Sequence of amplified Raman spectra and Lorentzian fits in range between 520 and 670 cm^{-1} showing the evolution of the E_g (ν_2) and A_{1g} (ν_1) Raman modes along the points 6→13 in panel (a). On the right of each spectrum, a scheme represents its contribution to the domain structure (i.e. a-domain, a/c-domain wall and c-domain). (c) Evolution of the A_{1g}/E_g ratio measured along the points 6→13 in the panel (a). The A_{1g}/E_g ratio is used to determine the polarization orientation of each domain, showing that KNN-based polycrystalline exhibits an a/c/a/c-like domain structure, made up of out-of-plane polarized c-domains (maximum value of the A_{1g}/E_g ratio) and in-plane polarized a-domains (minimum value of the A_{1g}/E_g ratio). (d) Evolution of the Raman shift of the A_{1g} mode showing the existence of a strain gradient into the ferroelectric domains, which reaches a maximum at a/c-domain wall (evolution represented by a red arrow), and a minimum at c/a-domain wall (evolution marked with a blue arrow). (e) Schematic illustration of the ferroelectric polarization gradient on the domain structure. The a/c-domain wall is correlated to a head-to-head 90° domain wall, causing a strongly charged wall (sCDW). The c/a-domain wall has a tail-to-tail configuration resulting in weakly charged domain walls (wCDW). Polarization directions are indicated by 3D arrows.

The presence of strain gradients evidences the presence of DWs which are not electrostatically neutral. The

DWs located at both maximum and minimum strain values are special cases of violation of the electrostatic neutrality,³⁷ resulting in the formation of “charged domain walls” (CDWs). These singular CDWs have been demonstrated both in thin films³⁸⁻⁴⁰ and single crystals¹⁴, and recently in KNN ceramics – the subject of this study.⁴¹ Moreover, the mechanical writing of charged conducting walls through locally applied point-stress has been recently reported in $\text{Cu}_3\text{B}_7\text{O}_{13}\text{Cl}$ single crystals.⁴²

DWs located at maximum strain values should be categorized into a type of CDWs denominated strongly charged walls (sCDW), typically having a head-to-head configuration, while those DWs detected at low strain values can be classified as weakly charged domain walls (wCDW), typically of tail-to-tail configuration.⁴³ The effect of CDWs on the Raman shift of the A_{1g} mode is quite relevant. The out-of plane polarization regions show higher force constants indicating higher displacement of the Nb^{5+} cation from the electrostatic equilibrium position in the oxygen octahedra. Thus, the larger the Raman shifts the higher the piezoelectric response.³⁰ By the contrary, the in-plane polarization regions show Raman redshift due to strain constrictions. The presence of CDW enhances the octahedra distortion, and hence locally contributes to the Raman blueshift, meanwhile the wCDW reduces the polarization. The strain gradient across the alternate needle domains results in a combination of out-plane and in-plane polarization regions with the modulation of CDWs (**see supporting information S3**).

So far, we have demonstrated the existence of strain gradients in $a/c/a/c$ -like domain structure transiting from maximum to minimum strain states, which are localized at a/c - and c/a -domain walls, respectively (*see schematic illustration of Fig. 2e*). In addition, a correlation between BO_6 distortion and the remnant polarization (P_r) in KNN-based ceramics has been shown by studying the Raman spectroscopy.³⁰ From the linear relationship existent between the A_{1g} Raman mode shift and P_r ,³⁰ we infer that the observed shift of 4 cm^{-1} in **Fig. 2d** corresponds to a P_r variation larger than 20%. Thus, we can establish the existence of a polarization gradient increasing at the a - c -DWs.⁴⁴ The greater Raman shift is an indirect proof of the electric field enhancement created at the head-to-head (**H-H**) a - c -domain wall (**Fig. 2e**). Conversely, the tail to tail configuration (**T-T**) at the c - a -DWs exhibits the minimum strain state and, consequently, a lower polarizability. In accordance with the observations of *Gao et al.*,⁴⁵ the a - c -domain wall is a transition zone of mixed polarization, in which is observed that the a -domain (at left of the a/c domain wall) show the higher polarization, transiting to minimum polarization state along the c -domain. In other words, this means that the polarization transition zone is located close to the a/c domain wall whose role is to minimize the charge density. This latter configuration perfectly agrees with the conductivity behavior recently predicted by Setter’s group,⁴³ - See schematic

illustration of the **Fig. 2e**, as well as with the elastic compatibility conditions between specific domain pairs reported in reference 42. Further, the results are consistent with recent works based on PFM experiments where the presence of CDWs in KNN was experimentally confirmed for large grain sizes (1-10 μm) by means of PFM experiments.⁴¹

On the basis of the above analysis, we can establish a phenomenological set of features that are of great importance to find CDWs in ceramics. Firstly, the CDWs appear in large grains since for small grain sizes⁴¹ ($< 1 \mu\text{m}$), the grain boundary limits the formation of non-180° domains. The stress in the ceramics occurs as a consequence of the polymorphic phase transformation in a perovskite unit cell ABO_3 from paraelectric to ferroelectric state during cooling of the sintering process. The appearance of a polar direction introduced stress in the grains that could not be accommodated by 180° domains and requires polarization rotation by non-180° domains. If grain size is low enough the grain boundaries energy could avoid the formation of such non-180° domains. Recently, observations of *Esin et al.*⁴¹ by using PFM confirmed that the formation of non-180° domains are required to the formation of CDWs. Secondly, the domain wall density is higher than expected for the grain size found in our study. Domain width is smaller than predicted for ceramics (as it is evidenced in **Supplementary information S2**). This means that the formation of CDWs serve as a mechanism to accommodate large stresses than in regular domain structures. And finally, the ceramic in this study possesses a monoclinic symmetry (M_c) that allows the higher number of polarization directions so the switching of polarization. $\sim 90^\circ$ and $\sim 60^\circ$ domain switching could nucleate in the positions of the local stress to release elastic energies and therefore the internal stress in 180° domain switching could be effectively relaxed by establishing $\sim 90^\circ$ and $\sim 60^\circ$ domain stripe, as it is evidenced by *Deng et al.*⁴⁶ The domains in presence of CDWs show a structural gradient that support a polarization gradient, as it is evidenced in **Figure 2**.

2. 3. Imaging and Analysis of the Ferroelectric Domain Structure by Second Harmonic Generation Microscopy

Having characterized and ascertained the capability of CRM method to resolve the nanoscale domains structure of the ceramic system, it is necessary to precisely locate the charged interfacial boundary by a more specify technique, such as Second Harmonic Generation (SHG) microscopy. It is well established that different crystallographic orientations of the spontaneous polarization result into noticeable variations of the SHG intensity because of the restrictive symmetry rules that governs the quadratic nonlinear processes. Hence, by scanning laterally the sample with the fundamental beam it should be possible to distinguish between the *in*

plane (*a*-domain) and *out of plane* (*c*-domain) domain structure present in the KNN ceramic. Further, the superior sensitivity of SHG to subtle changes in the crystal symmetry would also allow to detect any local inhomogeneous strain in the system,⁴⁷ providing a complementary tool to Raman spectroscopy imaging for unraveling the presence of charged domain walls.

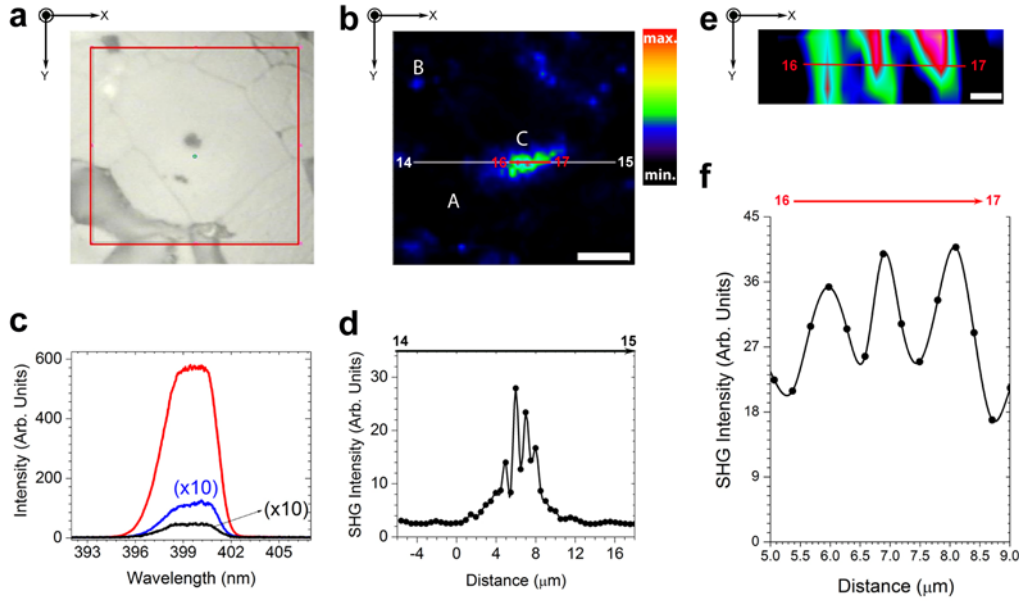


Figure 3 | Imaging and Analysis of the Ferroelectric Domain Structure in KNN by Second Harmonic Generation Microscopy. (a) Optical micrograph of the spatial area scanned by SHG. (b) SHG microscopy image displaying the *in plane* (black color) and *out of plane* (blue color) ferroelectric domain structure present in the KNN ceramic. The contrast in the image arises from the different SHG intensity values obtained when different tensor components (nonlinear coefficients) are involved in the nonlinear process. Scale bar: 3 μm. (c) SHG spectra recorded at the *a*-domains (black line), *c*-domains (blue line,) and the central region of the grain where the strongest nonlinear response (SHG intensity) was monitored (red line). For the sake of comparison, the SHG spectra collected at the isolated *a/c* ferroelectric domains have been multiplied by a factor of x10. (d) SHG intensity profile obtained by integrating the total emitted area as a function of the spatial position across the line denoted as 14→15 in panel (b). (e) Spatially resolved SHG image recorded at the central region of the grain with a larger magnification. The colour code reflects the intensity variations across the striped-like nanodomains. Scale bar: 0.5 μm. (f) SHG intensity profile obtained across the striped-like ferroelectric domains displayed in panel (e). The scanned line has been denoted as 16→17.

Figure 3 shows the optical (**Figure 3a**) and SHG image (**Figure 3b**) obtained when scanning the same spatial region analyzed by Raman spectroscopy. For the experiments, the fundamental beam was polarized parallel to the x-axis in the figure. As expected, the spatial map of the SHG intensity reveals the presence of the two types of ferroelectric domains in the sample (black and blue color in the image), their contrast generated by the different nonlinear coefficients (tensor components probed by the incident beam) involved in the SHG process. Additionally, a well-defined area showing a much stronger SHG signal is clearly distinguished at the central region of the image. **Figure 3c** depicts the SHG spectra recorded at the three regions of interest: *a*-domains (black line), *c*-domains (blue line,) and the central region of the image, where the strongest nonlinear response (SHG intensity) was observed (red line). For illustrative purposes, these regions have been marked

in **Figure 3b**, by A, B and C, respectively. As observed, the SHG intensity collected at the central region is about one order of magnitude higher than that obtained at the isolated *a/c* ferroelectric domains. Further, as illustrated in **Figure 3d**, the SHG intensity profile across this spatial region is composed of a peak-valley structure with a separation between the maxima of about 1 μm .

To get further insights into this aspect, **Figure 3e** shows a close-up view of the SHG scan in the central region. As seen, the periodical spatial modulation of the SHG intensity can be directly related to the formation of ultrafine striped-like ferroelectric domains of about 500 nm width, in good agreement with the Raman results (**Figure 1**). Moreover, as illustrated by the color code in the Figure, the SHG intensity across the striped-like nano-domains is not uniform, but shows a spatial gradient. The oscillating trend of the nonlinear response across the nano-domain structure is further illustrated by the SHG intensity profile shown in **Figure 3f**. Note that SHG signal initially increases at the first nano-domain, then reaches a maximum at the domain wall boundary and decreases in the subsequent nano-domain until reaching the next wall. Such spatial distribution is consistent with the different strain fields associated with the stripped needle-like ferroelectric domains, and indicates that the maximum and minimum values of the gradient are spatially localized at domain walls.

2. 4. Relevance of Charged Domain Walls in the Domain Switching Mechanism

A relevant feature of ferroic materials is the possibility of an active control of their functionalities at the nanoscale via external stimuli such as applied stress, magnetic or electric fields, and in this particular case, polarized light. In situ observations of polarization switching were carried out by illuminating with polarized light. **Figure 4a-g** display the evolution of the Raman images of the surface of the KNN ceramics in which ferroelectric domains shift along the X axis. The 18→19 line serves as a reference guide to follow the domain movement. From **Fig. 4a-g**, one can deduce that the light polarization direction alters the Raman modes. The Raman spectrum of the red-domain (*i.e. out-of-plane polarized c-domain*) evolves toward blue-domain (*i.e. in-plane polarized a-domain*), which account for a structural change.

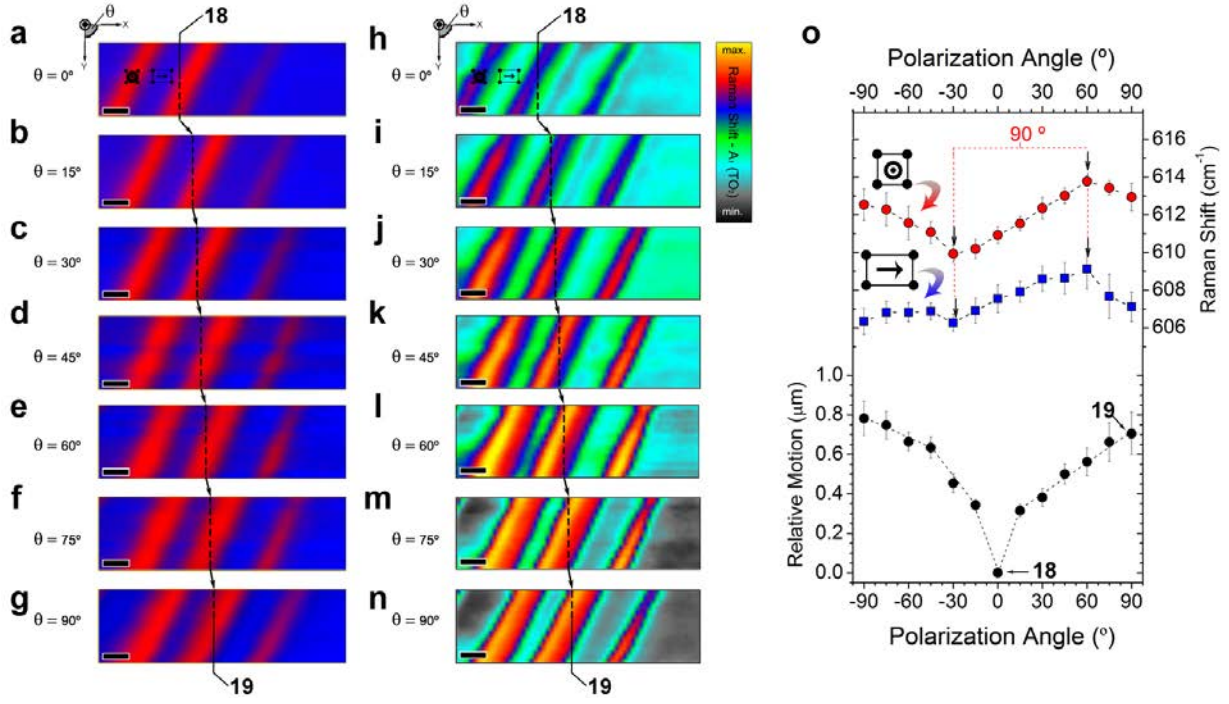


Figure 4 | Light-Controlled Ferroelectric Domain Switching in Polycrystalline Ferroelectric. (a-g) Set of Raman images showing the switching of the domain structure of the KNN surface section (area marked as 3 in Fig. 1c), for light polarization angles between $-90^\circ \rightarrow 0^\circ \rightarrow 90^\circ$. Red regions denoted out-of-plane polarization or *c*-domain, and blue regions denoted in-plane polarization or *a*-domain. The scheme at the top of the Fig. 4a represents the coordinates where the light polarization angle θ at the surface of the crystal varies in the plane XY. Additionally, the value of the light polarization angle θ is indicated on the left side of each Raman image. Scale bar, 500 nm. (h-n) A collection of Raman shift images showing the strain evolution on the ferroelectric domain structure. The relative motion of domains is illustrated along the line marked as 18 \rightarrow 19. (o) Evolution of the A_{1g} Raman shift for two principal adjacent domains (*i.e.* an in-plane polarization or *a*-domain, signaled in blue and an out-of-plane polarization or *c*-domain, signaled in red,) as a function of the light polarization angle. The error bars show the standard deviation (*sd*) of the Raman shift evolution for three main points in the domain structure for each angle of light polarization on a given sample. The relative change position of domain is showed along the line marked as 18 \rightarrow 19 in h-n, and is also depicted as a function of the polarization angle (θ) at the bottom of (o). The error bars correspond to the *sd* of the relative motion.

In order to further determine the strain degree, and consequently, as shown in Fig. 2d, its polarizability degree associated with the domain moving, the Raman shift image of the A_{1g} Raman mode for each light polarization angle is also displayed in Figs. 4h-n. Both the *a*-domain and *c*-domain show a maximum Raman shift for a light polarization angle of 60° , coinciding with the DWs. A minimum Raman shift is observed for a light polarization angle of 30° , at the direction perpendicular to the DWs. Moreover, the Raman shift differences between the in-plane and out-of-plane polarization region show a minimum at -30° and a maximum at 60° , as a proof of the strain evolution with the angle of polarization of the light (θ). So, the Raman shift changes with the light polarization angle and the DW motion are correlated to the light polarization angle. (See Fig. 4h-n) Fig. 4o shows the influence of the light polarization angle on the final domain position. The relative motion is plotted by using as reference the line marked as 18 \rightarrow 19 in Fig. 4a-g and 4h-n, respectively. In this way, we can infer that the relative motion of the domains is approximately 780 ± 90 nm when rotating the polarization

from 0 to 90°. More specifically, the anisotropic strain (evidenced in **Fig. 2d**), is correlated with alternating strongly and weakly charged domain walls, playing a key role in the ferroelectric domain switching.

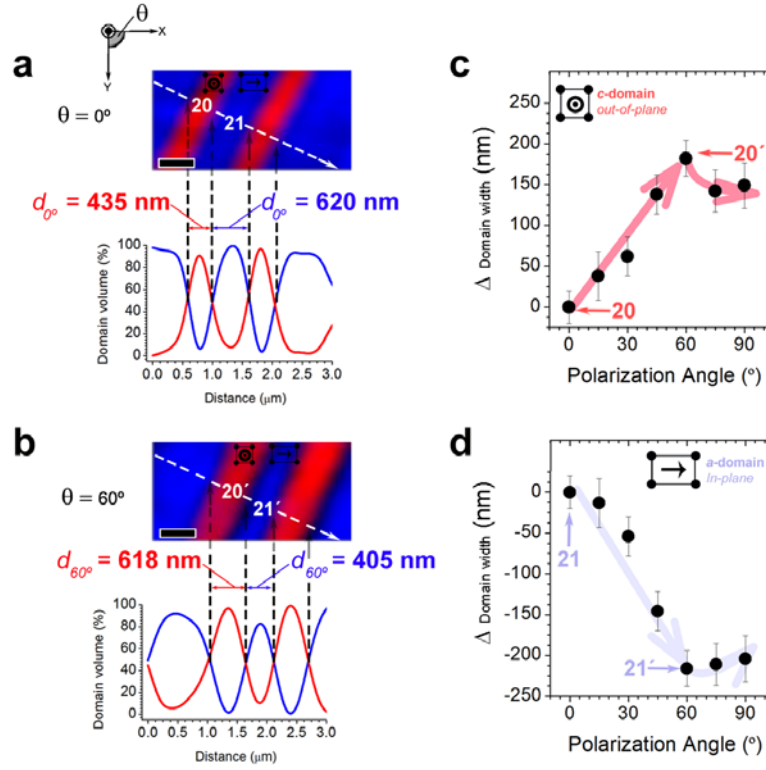


Figure 5 | Influence of the polarized light on the domain width. (a-b) Spatial map of the Raman signal showing the domain structure at the surface by colour code, which corresponds to θ of 0° and 60° , respectively. Scale bar, 500 nm. A line-scanned profile of the relative volume of each ferroelectric domain is plotted at the bottom of each image (indicated by the white dashed arrows). (c) Relative domain width evolutions for the *c*-domain (indicated with 20 and 20' in panels a-b) and (d) for the *a*-domain (signaled with 21 and 21' in panels a-b) plotted as a function of the polarization angle θ . The error bars show the *sd* of the relative motion.

Moreover, the domain switching mechanism is evidenced by the clear evolution of the domain width (d) observed in **Fig. 4**. A depth analysis of the evolution of d is shown in **Figure 5**. The two relevant cases corresponding to $\theta = 0^\circ$ and $\theta = 60^\circ$ are depicted in **Figs. 5a-b**, respectively. We find a remarkable correlation between the increased d corresponding to out-of-plane polarized *c*-domains (that is, a dimensional change) and the tuning of the light polarization angle; see *c*-domain indicated with 20 and 20' on the **Figs. 5a-b**. The line scan profile of phase volume for each domain in **Fig. 5a** shows an oscillatory behavior, perfectly correlated with the *a/c/a/c*-like domains structure. It is formed by out-of-plane polarized *c*-domains (red color) and in-plane polarized *a*-domains (blue color) separated by a 90° domain wall (determined by the intersection between the two curves shown in line profile of **Fig. 5a**). In **Fig. 5c**, we plot the relative growth of d for a *c*-domain (indicated with 20 and 20') as a function of θ . This analysis shows that the d growth is approximately $183 \pm 30 \text{ nm}$ when θ changes from 0 to 60° . It is worth to notice that at $\theta \approx 60^\circ$ the electric field of the polarized light is nearly parallel to the domain walls. As expected, the adjacent *a*-domain undergoes a proportional

decrease in d , which is indicated with 21 and 21' in **Figs. 5a-b** (its relative growth is plotted in blue color in **Fig. 5d**). The results provide a conclusive proof that a light-induced local electric field is able to perform 90° domains switching, thereby modifying the domain dimension.

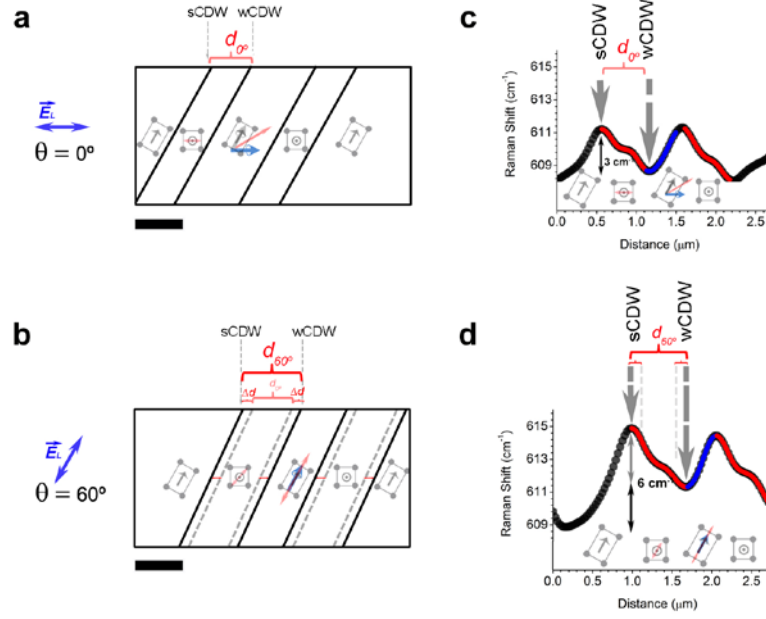


Figure 6 | Charge Domain Walls Effect on Light-Driven Domain Switching Mechanism. (a-b) Schematics of the main contributing polarization directions with their respective polarization vectors for the special cases $\theta = 0^\circ$ (a), and $\theta = 60^\circ$ (b). The scale bar for both panels (d) and (e) is 500 nm. The direction of the blue, grey and red arrows depicts the light polarization, polarization vector and the resulting macroscopic polarization. The solid line represents the DWs at $\theta = 0^\circ$ (d), and $\theta = 60^\circ$, while dashed line shows the relative d growth for a c -domain by means of θ variation from $\theta = 0^\circ$ to $\theta = 60^\circ$. In the schematic representation showing a strongly charged wall (sCDW), which is related to a head-to-head 90° domain wall. Whereas the weakly charged domain walls (wCDW) has a tail-to-tail. Besides, the value of θ and its light polarization direction (marked with a blue double arrow) are indicated on the left side of each scheme. Line-scanned profile of the Raman shift of the A_{1g} mode for the cases $\theta = 0^\circ$ (d), and $\theta = 60^\circ$ (e). Line-scanned profiles correspond to the white dashed arrows of the Figs. 5a-b.

Before concluding, it is worth considering that the effect presented in this work can be explained with the scheme shown in **Figures 6a-b**. One of the main aspects to take into account is the slight DW mismatch between the two ferroelectric domains, which triggers the formation of sCDW. Locally, the formation of sCDW may vary substantially the net polarization into each domain, resulting on a strain gradient. The formation of strain patterns also affects the light-driven domain switching mechanism. Upon polarized light illumination non-180° domain switching occurs and produces a net dimensional change (with respect to the initial state) along the light polarization direction compatibly to the orientation of the domains. As the crystal structure is monoclinic, Mc type, the Ps can rotate in a direction between the tetragonal and the orthorhombic polar crystallographic directions. In particular, the monoclinic phase Mc is defined by a polarization direction that deviates from any of the 12 orthorhombic polarization directions by more than 5° .⁴⁸ Under the electric field associated with the polarized light, the monoclinic polar directions are able to move in order to relieve the crystal

stress imposed by the domain walls. The occurrence of multiple polar directions in the monoclinic phase favors the Ps rotation. The electric field of the polarized light allows enhancing the ferroelectric polarization as it is stated from the blueshift of the Raman mode A_{1g} . It is interesting to point out that the same behaviour is displayed in both Raman shift evolution (**Figs. 6c-d**) (*that is, strain evolution*) and relative d growth (**Figs. 5c-d**) versus the light polarization angle (θ). In other words, the strain evolution and the relative growth, d , first increase and then slightly decrease as θ increases, reaching a maximum for $\theta = 60^\circ$. As the domain width increases when the direction of the polarized light is almost parallel to the domain wall, two aspects contributes to the enhancement of the ferroelectric polarization revealed by the Raman blueshift: the stress relief and the enhancement of the CDW effect. Moreover, the variation in the angle of the polarized light respect to the crystallographic polar directions produces a variation in charge at the CDWs equal to the variation of the electric field. The evolution of polarization with the domain switching provides a conclusive proof that a light-induced local electric field is able to 90° domain switching modifying the domain dimension. Thus, the alignment of light polarization direction with the domain wall produces a variation in charge at the CDWs similar to a variation of the electric field. *The reader can find a schematic representation showing the effect of electrical field application on a polycrystalline ferroelectric with random orientated grains in **Supplementary information S4**.*

Summarizing, the c -domain shows a width increase when the polarized light is parallel to the DW's indicating that the effect of light is similar to the application of an electric field in the *out-of-plane* polarization direction. In addition, the width increasing of the *out-of-plane* polarization when the polarized light is parallel to the DW's could only be correlated with the charge variation across the CDWs, and therefore the effect of the associated local electric field. The polycrystalline material considered in this work, with imperfect DW matching between the individual domains, is obviously a non-idealized structure. Thus, the analysis of its optical fingerprints presented here is an essential step forward in view of identifying and understanding the features of real systems.

3. Conclusion

To conclude, utilizing combination of quantitative CRM with SHG analysis, we have demonstrated the existence of stable CDWs in polycrystalline ceramics by using a prototypic KNN based material having monoclinic phase. The CDWs are located in large grains having larger density of domain walls than that predicted from the grain size rule.³⁶ It is shown that the presence of CDWs is not exclusive to exotic systems

since they are commonly present in ceramic materials. The ferroelectric domains possess strain gradients as a consequence highly charged CDWs characteristic of head-to-head configuration, meanwhile low charged CDWs correspond to tail-to-tail configuration. The domain motion of CDWs is attained through the variation of the polarization angle of the incident light. Coupling of polarized light with the ferroelectric structure produced a variation of the crystallographic polar direction that explains the domain motion due the strain change experimented by the ferroelectric regions. In addition, the alignment of light polarization direction with the domain wall produces a variation in charge at the CDWs equal to the variation of the electric field. In the present work the domain wall motion has been achieved only by the application of polarized light without electric contacts or external electric field, resulting, thus, in a relevant approach to nano-domain motion control in new optoelectronic nanodevices. It is important to point out that light-driven ferroelectric domain switching can be modulated through the light polarization angle control. Moreover, this approach opens new possibilities to understand both the generation of ferroelectric domains and the dynamics of domain motion in piezoelectric ceramic materials. These findings point the way towards more stable device designs based on large-scale production of ferroelectric materials.

4. Experimental Section

Sample Preparation: For the preparation of $K_{0.1}Na_{0.9}NbO_3$ (KNN) precursor, a 10 M alkaline solution is prepared keeping the molar ratio potassium hydroxide (KOH, 99.0%, Sigma-Aldrich)/ sodium hydroxide (NaOH, 99.5%, Sigma-Aldrich) on 7.5:2.5 in DI water. After then, 2 grams of the niobium oxide (Nb_2O_5 , 99.999%, Sigma-Aldrich) and cetyltrimethylammonium bromide (CTAB, Sigma-Aldrich) is added to the mixture with additional vigorous for 2 h. The resulting suspension is placed into a Teflon lined autoclave, and the reactor is deposited inside a microwave oven (MARS model, CEM corporation), which is heated at 190 °C for 30 min. Upon reaction completion, the precipitate resulting is washed several times with DI water and dried at 120 °C for 2h. With the objective of achieving a sintered sample, the dried ceramic powders were uniaxially pressed under 200 Mpa in a disk-shaped. Then, the disk-shaped compact is sintered at 1125 °C for 2 h in air atmosphere, obtaining a density of 4.35 g/cm³. A standard KNN microstructure was observed from Field Emission Scanning Electron Microscopy (FE-SEM, Hitachi S-4700), **Fig. S2a**. Note that the sintered sample is composed by grains with platelet morphology, which present an average grain size of $\sim 6.7 \pm 3 \mu m$, see **Fig. S2b**. In addition, one can establish that the domain width (d) can be roughly expressed by the correlation: $d \sim \sqrt{a}$ (that is, domain widths, d , scale as the square root of the grain size, a),^{6,36} meaning that for an average grain size of $a \sim 6.7 \mu m$ (our case) the d value should be ca. 2.5 μm , as shown in **Fig. S2c**.

In order to analyse the domain structure, the ceramic sample was polished and thermally etching to reveal the topography. With this purpose, the surface of the pellets was carefully polished in two steps. The first step consisted in a “hard polishing” or grinding process using Silicon carbide abrasive papers (MetaServ® 250 Grinder-Polisher, BUEHLER, An ITW Company). This first step was carried out for each pellet in order to obtain parallel surfaces. Finally in a second step, the surface of the pellet was softly polished with diamond paste to obtain mirror finish surfaces using a VibroMet® 2 Vibratory Polisher (BUEHLER, An ITW Company). In consequence, the micro-roughness is inhibited resulting in an improvement of the sample surface finish. Finally, the ceramic sample was etched at 950 °C for 5 min to reveal the grain boundary of the microstructure. The sample was maintained at $T > 25^\circ C$ during the Confocal Raman Microscopy (CRM) measurements using a temperature controller. The identification of the crystal structure (monoclinic symmetry) and orientations of the KNN ceramic was accomplished by means of high-resolution synchrotron X-ray diffraction. Synchrotron radiation X-ray diffraction (SR-XRD) was recorded at the D10B-XRD1 beamline at the National Synchrotron Light Laboratory (LNLS, Campinas, Brazil) on an as-prepared sample mounted on a ceramic sample holder. The X-ray wavelength was set at 1.033200(1) Å, and data were collected in the range $1.208^\circ \leq 2\Theta \leq 121.180^\circ$ with a step length of 0.004° and a step counting time of 2 s using photon energy of 12 keV at room temperature. The refined wavelength using NIST LaB6 standard reference material was of 1.033200(1) Å. *More information about Rietveld refinement can be found in Supporting Information 1.*

CRM domain mapping. The experiments were conducted by Confocal Raman Microscope (CRM) coupled with Atomic Force Microscopy (AFM, Witec alpha-300RA) on polished ceramic. Raman spectra were collected using a 532 nm excitation

laser and a 100x objective lens (NA = 0.95). The incident laser power was 20 mW. The lateral and vertical resolutions of the confocal microscope were about ~250 nm and ~500 nm, respectively. The spectral resolution of the Raman system was down to 0.02 cm⁻¹. The microscopy sample was mounted on a piezo-driven scan platform having 4 nm lateral and 0.5 mm vertical positional accuracy. The piezoelectric scanning table allows steps of 3 nanometres (0.3 nm in the vertical direction), giving a very high spatial resolution for the Confocal Raman Microscopy. The microscope base was also fitted with an active vibration isolation system, active 0.7–1000 Hz. Collected spectra were analyzed by using Witec Control Plus Software.

Second Harmonic Generation (SHG) microscopy: Spatially resolved SHG experiments were performed on a customized scanning confocal microscope (Olympus BX41) provided with a two-axis XY motorized platform (0.2 μm spatial resolution) driven by Labspec software. A tuneable femtosecond Ti:sapphire laser (Spectra Physics Model 177-Series), used as a fundamental beam, was focused onto the sample surface by using both, 50x and 100x microscope objectives. The SHG signal was collected in backscattering geometry with the same objective and detected by a Peltier cooled photomultiplier tube. The fundamental wavelength was fixed at 800 nm.

Angular dependence. The *in situ* domain switching was monitored taking subsequent surface-scans at different polarization angles of the same area, using as position reference a significant point of the sample surface visible with the optical microscope. Surface scan Raman images had 5 μm of length, 1.5 μm of width, 100 x 30 spectra of 0.2 seconds of integration time at 20 mW of laser power. Thus, the Raman image consisting of 100 x 30 pixels (3000 spectra) required ~ 10 minutes for acquisition of the whole surface-section. Additionally, in order to avoid the photoconductivity effects present in KNN, in our experiments a polarized light with a wavelength (at $\lambda = 532$ nm) outside the two absorption maxima^{18,19} is chosen and the open circuit configuration is selected. The angle between the polarization of light and the scan direction by using $\Delta\theta = 15^\circ$ between $\theta = -90^\circ$ and $\theta = 90^\circ$ was rotated. The acquired spectra set were analyzed by using Witec Control Plus Software.

Domain width as a function of the light polarization angle (θ). In CRM, in-plane polarized a-domains and out-of-plane polarized c-domains exhibit spectra with unique features. This fact allows the separation of the signals, and hence, it also helps to determine the domain width evolution as a function of the polarization angle (θ). For that, the relative volume fraction of each ferroelectric domain was calculated by means Witec Control Plus Software along the different lines for each angle of light polarization on a given sample. Raman spectra for each ferroelectric domain can be compared qualitatively and quantitatively allowing to calculate the domain width (d). By scanning the ferroelectric domain structure and collecting the complete Raman spectrum at every spot, we can subsequently filter specific spectral data for a spatially resolved data point and construct both false-colour 2D map as well as a line-scanned phase volume profile plot of each domain as a function of the θ .

References

1. K. J. Choi, M. Biegalski, Y. L. Li, A. Sharan, J. Schubert, R. Uecker, P. Reiche, Y. B. Chen, X. Q. Pan, V. Gopalan, L.-Q. Che, D.C. Schlom, C.B. Eom, *Science*, 2004, **306**, 1005–1008.
2. J. Seidel, L. W. Martin, Q. He, Q. Zhan, Y.-H. Chu, A. Rother, M. E. Hawkrigde, P. Maksymovych, P. Yu, M. Gajek, N. Balke, S. V. Kalinin, S. Gemming, F. Wang, G. Catalan, J. F. Scott, N. A. Spaldin, J. Orenstein, R. Ramesh, *Nat. Mater.*, 2009, **8**, 229–234.
3. L. J. McGilly, P. Yudin, L. Feigl, A. K. Tagantsev, N. Setter, *Nat. Nanotechnol.*, 2015, **10**, 145–150.
4. J. C. Agar, A. R. Damodaran, M. B. Okatan, J. Kacher, C. Gammer, R. K. Vasudevan, S. Pandya, L. R. Dedon, R. V. K. Mangalam, G. A. Velarde, S. Jesse, N. Balke, A. M. Minor, S. V. Kalinin, L. W. Martin, *Nat. Mater.*, 2016, **15**, 549–556.
5. J. Gonnissen, D. Batuk, G. F. Nataf, L. Jones, A. M. Abakumov, S. Van Aert, D. Schryvers, E. K. H. Salje, *Adv. Funct. Mater.*, 2016, **26**, 7599–7604.
6. G. Catalan, J. Seidel, R. Ramesh, J. F. Scott, *Rev. Mod. Phys.*, 2012, **84**, 119–156.
7. M. Schröder, A. Haußmann, A. Thiessen, E. Soergel, T. Woike, L. M. Eng, *Adv. Funct. Mater.*, 2012, **22**, 3936–3944.
8. B. S. Kwak, A. Erbil, B. J. Wilkens, J. D. Budai, M. F. Chisholm, L. A. Boatner, *Phys. Rev. Lett.*, 1992, **68**, 3733–3736.
9. W. Eerenstein, N. D. Mathur, J. F. Scott, *Nature*, 2006, **442**, 759–765.
10. N. A. Mathur, *Nature*, 2008, **454**, 591–592.
11. N. Liu, R. Dittmer, R. W. Stark and C. Dietz, *Nanoscale*, 2015, **7**, 11787–11796.
12. D. Gobeljic, V. V. Shvartsman, A. Belianinov, B. Okatan, S. Jesse, S. V. Kalinin, C. Groh, J. Rödel and D. C. Lupascu, *Nanoscale*, 2016, **8**, 2168–2176.
13. P. Wang, J. Zhao, L. Wei, Q. Zhu, S. Xie, J. Liu, X. Meng and J. Li, *Nanoscale*, 2017, **9**, 3806–3817.
14. T. Sluka, A. K. Tagantsev, P. Bednyakov, N. Setter, *Nat. Commun.*, 2013, **4**, 1808.
15. G. De Luca, M. D. Rossell, J. Schaab, N. Viart, M. Fiebig, M. Trassin, *Adv. Mater.*, 2017, **29**, 1605145.
16. F. Rubio-Marcos, A. Del Campo, P. Marchet, J. F. Fernández, *Nat. Commun.*, 2015, **6**, 6594.
17. K. Uchino, S. Nomura, *Ferroelectrics*, 1983, **50**, 191–196.
18. K. Uchino, *Mat. Res. Innovat.*, 1997, **1**, 163–168.
19. D. Dimos, W. L. Warren, M. B. Sinclair, B. A. Tuttle, R. W. Schwartz, *J. Appl. Phys.*, 1994, **76**, 4305–4315.
20. V. M. Fridkin, New York: Consultants Bureau (1980).
21. V. M. Fridkin, A. A. Grekov, E. A. Savtchenko, T. R. Volk, *Journal de Physique Colloques*, 1972, **33 (C2)**, 127–129.
22. E. I. Bondarenko, V. Y. Topolov, A. V. Turik, *Ferroelectr. Lett.*, 1991, **13**, 13–19.
23. G. Arlt, N. A. Pertsev, *J. Appl. Phys.*, 1991, **70**, 2283.
24. S. Li, A. S. Bhalla, R. E. Newnham, L. E. Cross, *Mater. Lett.*, 1993, **17**, 21–26.
25. T. Rojac, H. Ursic, A. Bencan, B. Malic, D. Damjanovic, *Adv. Funct. Mater.*, 2015, **25**, 2099–2108.
26. J. Tellier, B. Malic, B. Dkhil, D. Jenko, J. Cilensek, M. Kosec, *Solid State Sci.*, 2009, **11**, 320–324.
27. A. S. Everhardt, S. Matzen, N. Domingo, G. Catalan, B. Noheda, *Adv. Electron. Mater.*, 2016, **2**, 1500214.
28. F. Rubio-Marcos, A. Del Campo, R. López-Juárez, J. J. Romero, J. F. Fernández, *J. Mater. Chem.*, 2012, **22**, 9714–9720.
29. K. Kakimoto, K. Akao, Y. Guo, H. Ohsato, *Jpn. J. Appl. Phys.*, 2005, **44**, 7064–7067.
30. F. Rubio-Marcos, M. A. Bañares, J. J. Romero, J. F. Fernández, *J. Raman Spectrosc.*, 2011, **42**, 639–643.
31. W. J. Merz, *Phys. Rev.*, 1954, **95**, 690–698.
32. E. K. W. Goo, R. K. Mishra, G. Thomas, *J. Appl. Phys.*, 1981, **52**, 2940–2943.
33. Z. Kighelman, D. Damjanovic, M. Cantoni, N. Setter, *J. Appl. Phys.*, 2002, **91**, 1495–1501.
34. M. Soga, Y. Noguchi, M. Miyayama, H. Okino, T. Yamamoto, *Appl. Phys. Lett.*, 2004, **84**, 100–102.
35. Y. L. Li, S. Choudhury, Z. K. Liu, L. Q. Chen, *Appl. Phys. Lett.*, 2003, **83**, 1608–1610.
36. G. Arlt, *J. Mater. Sci.*, 1990, **25**, 2655–2666.
37. T. Sluka, A. K. Tagantsev, D. Damjanovic, M. Gureev, N. Setter, *Nat. Commun.*, 2012, **3**, 748.

38. P. Maksymovych, A. N. Morozovska, P. Yu, E. A. Eliseev, Y.-H. Chu, R. Ramesh, A. P. Baddorf, S. V. Kalinin, *Nano Lett.*, 2012, **12**, 209–213.
39. I. Stolichnov, L. Feigl, L. J. McGilly, T. Sluka, X.-K. Wei, E. Colla, A. Crassous, K. Shapovalov, P. Yudin, A. K. Tagantsev, N. Setter, *Nano Lett.*, 2015, **15**, 8049–8055.
40. A. Crassous, T. Sluka, A. K. Tagantsev, N. Setter, *Nat. Nanotechnol.*, 2015, **10**, 614.
41. A. A. Esin, D. O. Alikin, A. P. Turygin, A. S. Abramov, J. Hreščak, J. Walker, T. Rojac, A. Bencan, B. Malic, A. L. Kholkin, and V. Ya. Shur, *J. Appl. Phys.* 2017, **121**, 074101.
42. R. G. P. McQuaid, M. P. Campbell, R. W. Whatmore, A. Kumar, J. Marty Gregg, *Nat. Commun.*, 2017, **8**, 15105.
43. P. S. Bednyakov, T. Sluka, A. K. Tagantsev, D. Damjanovic, N. Setter, *Sci. Rep.*, 2015, **5**, 15819.
44. X. Wei, T. Sluka, B. Fraygola, L. Feigl, H. Du, L. Jin, C.-L. Jia, N. Setter, *ACS Appl. Mater. Interfaces*, 2017, **9**, 6539–6546.
45. P. Gao, J. Britson, J. R. Jokisaari, C. T. Nelson, S.-H. Baek, Y. Wang, C.-B. Eom, L.-Q. Chen, X. Pan, *Nat. Commun.* 2013, **4**, 2791.
46. H. Deng, H. Zhang, X. Zhao, C. Chen, X. Wang, X. Li, D. Lin, B. Ren, J. Jiao, H. Luo. *CrystEngComm*, 2015, **17**, 2872–2877.
47. T. T. A. Lummen, Y. Gu, J. Wang, S. Lei, F. Xue, A. Kumar, A. T. Barnes, E. Barnes, S. Denev, A. Belianinov, M. Holt, A. N. Morozovska, S. V. Kalinin, L.-Q. Chen, V. Gopalan, *Nat. Commun.*, 2014, **5**, 3172.
48. Y. Gu, F. Xue, S. Lei, T. T. A. Lummen, J. Wang, V. Gopalan, L. Q. Chen, *Phys. Rev. B*, 2014, **90**, 024104.

Acknowledgments

This work was supported by the Spanish Ministry of Economy and Competitiveness (MINECO) under projects MAT2013-48009-C4-1-P, MAT2013-43301-R and MAT2016-76106-R, The Spanish National Research Council (CSIC) under project NANOMIND CSIC 201560E068 and Comunidad de Madrid under grant S2013/MIT-2740. R. U. I would like to thank Dr. Xavier Turrillas of ICMAB-CSIC (Spain) and Dr. Luis. G. Martinez of IPEN-CNEN (Brazil) for their discussions about Rietveld analysis and LNLS for the synchrotron data measurement. F. R-M is also indebted to MINECO for a 'Ramon y Cajal' contract (ref: RyC-2015-18626), which is co-financed by the European Social Fund. L. R and R. P are also indebted to this work is carried out with funds from CONICET, ANPCyT, University of Mar del Plata (Argentina).

Author contributions

F. R-M. and J. F. F. designed and performed experiments, analyzed results and wrote the manuscript. A. D C. carried out Raman Image experiments and analyzed results. R. R-H. and R. U. I contributed to structural analysis. L. A. R. and R. P prepared the samples and contributed to data analysis. M. O. R. and M. L. B. contributed to SHG experiments.

Additional information

Competing financial interests: The authors declare no competing financial interests.

† Associated content

Electronic supplementary information (ESI) available.

Crystallographic characterization of KNN Ferroelectric Ceramic by High-resolution synchrotron X-ray diffraction; Microstructural characterization and domain width distribution of KNN ceramic calculated from the grain size measured by FE-SEM.

The Table Of Contents (TOC)

Keyword

Ferroelectric domain structure; Strain gradient; Charged domain walls; Optical-driven ferroelectric domain switching; Lead-free Piezoelectric ceramics materials

Title

Experimental Evidence of Charged Domain Walls in Lead-free Ferroelectric Ceramics: Light-driven Nanodomain Switching

ToC figure

The emergent phenomena driven by light-matter interaction may have potential applications in next generation domain wall nano-electronics utilizing polycrystalline ferroelectrics.

